JEAP
Journal of Environmental Analysis and Progress
ISSN: 2525-815X
10.24221/jeap.10.4.2025.7451.250-262

Evaluation of microporosity and density of carbonate rocks using gamma-ray and X-ray computed tomography techniques

Wellington da Silva Carvalho[a], Daniel Milian Pérez[a], Abel Gámez Rodríguez[a], Yaicel Ge Proenza[a], Patrício Luiz de Andrade[a], Daniel Amancio Duarte[a], Márcio Fernando Paixão de Brito[a], Cássia Bezerra Machado[a], Raquel Milani[a], Antonio Celso Dantas Antonino[a]

[a] Universidade Federal de Pernambuco-UFPE, Departamento de Energia Nuclear. Av. Professor Luiz Freire, n. 1000, Cidade Universitária, Recife, Pernambuco, Brasil. CEP: 50.740-545. E-mail: wellington.carvalho@ufpe.br, daniel.milian@ufpe.br, abel.rodriguez@ufpe.br, yaicel.geproenza@ufpe.br, patricio.andrade@ufpe.br, daniel.aduarte@ufpe.br, marcio.paixao@ufpe.br, cassia.bezerra@ufpe.br, raquel.milani@ufpe.br, antonio.antonino@ufpe.br.

ARTICLE INFO

Received 06 Nov 2024
Accepted 01 Oct 2025
Published 27 Dec 2025

ABSTRACT

Computed Tomography (CT) techniques have emerged as a promising non-destructive method to analyze the physical properties of rocks and porous media. CT techniques provide quantitative and qualitative information without disturbing the internal structure of the samples, which is a significant advantage for studies focused on understanding subsurface characteristics. This study investigated the potential and application of gamma-ray computed tomography (γ-CT) and X-ray microtomography (XR-μCT) for characterizing the microporosity and density of rocks, specifically carbonate rocks. Accurate characterization of these properties is crucial for evaluating water reservoir potentials, understanding geological formations, and assessing environmental impacts. The research aimed to validate the accuracy of both techniques and assess the feasibility of using a single XR-μCT projection to determine physical properties, potentially reducing computational demands. Validation involved samples with homogeneous, known composition, determining density and mass attenuation coefficients with both techniques, and comparing results to literature values. γ-CT achieved accuracy within 1.86%, while single-projection XR-μCT showed relative differences up to 10.65%. Subsequently, three carbonate rock samples were analyzed using XR-μCT with an average of four projections, improving accuracy over the single-projection method. Results from both CT techniques and literature values were compared, with γ-CT measuring parameters showing a relative difference of up to 4.58%, and the four-projection XR-μCT demonstrating strong accuracy. Relative differences in γ-CT were generally higher than XR-μCT, confirming the four-projection approach's significant improvements.

Keywords: Computed Tomography, gamma transmission, X-ray microtomography, carbonate rocks, porosity, density.

Introduction

Computed Tomography (CT) techniques and other industrial nuclear measurement systems fundamentally rely on the use of one or more radiation sources combined with one or more detection units. These systems pair radiation sources with detectors to monitor interactions with the target object or process. Valuable information can be obtained by assessing how ionizing radiation interacts with the material or process under study. Such measurements provide critical parameters for analyzing and evaluating the system or object under investigation (Abdullah et al., 2008). Among the array of CT techniques for industrial process studies, gamma-ray computed tomography (γ-CT) and X-ray microtomography (XR-μCT) stand out (Jacobs & Cnudde, 2009; Bjørnstad, 2021). Both are based on measuring the attenuation process of a photon flux during its interaction with the process or object under investigation (Martyushev et al., 2019, 2022, 2023ab, 2024).

These techniques are widely used in non-destructive studies of the physical properties of rocks and porous media (Geiger et al., 2009; Müter et al., 2012; Gurin et al., 2018; Fonseca et al., 2019; Al-Tersawy et al., 2021; Giamas et al., 2022; Saadat & Rahimpour-Bonab, 2023). Specifically, their application is essential in examining carbonate rocks, a sedimentary rock characterized by high porosity and density. These properties make them ideal for storing and facilitating the flow of hydrocarbons, which are critical to the oil and gas industry, sustainable water resource management, and environmental impact assessment. Accurate characterization of microporosity and density in carbonate rocks is crucial for understanding their potential as reservoirs for oil and water, optimizing resource extraction, and minimizing environmental impacts (Van Geet et al., 2000; Martínez-Martínez et al., 2016; Rahner et al., 2018; Galkin et al., 2022; Al-Yaseri et al., 2024). The characterization of rocks plays a fundamental role in geological-physical studies of caves and soils subjected to drilling and exploration, including rock formations of sandstones, quartzites, gneisses, mica schists, basalts, ferruginous formations, and alkaline volcanic rocks (Freire et al., 2017), as well as in studies of susceptibility and vulnerability to erosion (Melo et al., 2023).

While XR-μCT has a wide range of applications across scientific and industrial fields, underscoring its versatility, the present study focuses specifically on its use in the characterization of carbonate rocks. A brief overview of these broader applications is provided below to contextualize the technique's capabilities.

Recent studies detailing the applicability of XR-μCT-based techniques in geographical sciences and environmental studies are discussed below. Abbasi et al. (2022) used XR-μCT to visualize and analyze the 3D structure of natural gas hydrates in sediments, offering a powerful tool for understanding their formation, distribution, and impact on fluid flow. The use of this technique revealed how hydrates grow within different pore structures, providing insight into their filling modes and the influence of hydrate saturation on sediment mechanical properties. Chirol et al. (2021) applied XR-μCT and developed a robust segmentation method for quantifying pores, live roots, and necromass in complex wetland soils. This provides a comprehensive view of the 3D structure and interactions of these elements. The approach distinguishes live roots at the surface from necromass, enabling studies of soil functions such as cohesivity, nutrient exchange, and carbon dynamics. An et al. (2023) employed XR-μCT to visualize and quantify the development of drying-induced cracks in granite residual soil (GRS) under controlled desiccation conditions. The 3D reconstruction of cracks reveals that connected cracks play a key role in soil cracking and affect soil permeability. By comparing simulated and measured permeability values, the study validates the accuracy of seepage models and demonstrates the significant impact of desiccation on the hydraulic properties of GRS. Tötzke et al. (2024) used XR-μCT as a non-invasive approach to detect and analyze microplastic particles in sandy soil, even in organic materials. The combination of neutrons and X-rays allows unambiguous identification of microplastic particles and provides detailed information about their 3D shape, size, and distribution within the soil matrix. This technique opens new possibilities for studying the influence of microplastics on soil properties and plant-soil interactions. Martinez-Garcia et al. (2021) developed a novel automated method to extract 3D tree-ring structures and calculate tree-ring widths from XR-μCT data. This approach performed well on various wood species, including conifers, ring-porous, and diffuse-porous woods, offering a highly reproducible and efficient method for analyzing large datasets. Cloete et al. (2019) used XR-μCT to analyze the elemental content and microstructural features of roasted organic coffee beans from different regions, providing insights into their nutritional content, quality, and geographic origin. Although the study does not find a strong association between elemental profiles and production region, it suggests that soil-plant properties may influence regional elemental signatures. Khudhur et al. (2023) investigated the mechanisms and microstructures involved in slag's passive atmospheric CO_2 mineralization at ambient conditions, using various analytical techniques, including XR-μCT. The analysis revealed that the porous microstructure and the presence of åkermanite-gehlenite minerals play crucial roles in the CO_2 uptake process, with calcite being the main precipitated carbonate. This study provides a detailed understanding of the microstructural features that influence CO2 uptake and highlights the potential to optimize passive CO_2 mineralization in slag. León-Quinto et al. (2024) investigated the effects of cold on the inner and outer morphologies of neotropical pest larvae. XR-μCT plays a crucial role in characterizing the morphological changes associated with cold acclimation, specifically the reduction in hemolymph volume and the thickening of the integument. The study also investigates the levels of cryoprotectants, such as glycerol, trehalose, and glucose, in hemolymph. This research contributes to the understanding of the diverse strategies insects employ to survive cold temperatures, highlighting the complexity of insect cold adaptation.

Despite its extensive applicability, as discussed above, this study centers on comparing XR-μCT and γ-CT specifically for density and porosity analysis in carbonate rocks. The refinement of γ-CT and XR-μCT techniques for characterizing carbonate rocks is continually evolving to offer simpler sample preparation and more efficient image projection. This advancement enables precise, faster estimation of fundamental properties, such as porosity, moisture content, morphology, compaction level, permeability, and density, of soils and rocks. Estimates of microporosity and density obtained using CT techniques contribute to the classification of rock formations as siliciclastic or carbonate, with the latter being the focus of this investigation. For example, in siliciclastic rocks with aquifer-type porosity, mechanical processes predominate. In contrast, in carbonate rocks, the predominant porosity is of the aquifer type in a fissure medium (Paula & Rocha, 2021). Additionally, the literature includes applications of XR-μCT in oil recovery research for the nondestructive visualization of internal rock features and sediments (Peters & Afzal, 1992). In this context, CT imaging analysis of carbonate rocks using estimated linear and mass attenuation coefficients is essential for characterizing rock composition. The technique is based on obtaining a set of projections that represent the object irradiated. This set of images will represent the photon's attenuation coefficients of each material.

Despite its many advantages, XR-μCT faces challenges, notably the generation of large data volumes. This requires powerful computational capabilities for reconstruction and processing, often leading to significant delays and limiting the technique's broader application. Considering this, the present study proposed a novel approach to streamline XR-μCT analysis by exploring the feasibility of using only a reduced number of projections, potentially even a single forecast, to determine physical properties such as density and porosity.

While the versatility of XR-μCT has been extensively demonstrated in various fields, this work narrows the focus to carbonate rocks, aiming to contribute specifically to their radiometric characterization. The comparative analysis of γ-CT and XR-μCT in this geological context is particularly relevant given the economic and environmental importance of carbonate reservoirs.

The main scientific gap addressed here is the lack of comparative studies between γ-CT and XR-μCT for carbonate rocks, especially regarding the impact of projection number on accuracy and computational efficiency. By evaluating the potential for reducing projection numbers in XR-μCT without significant loss of accuracy, this study provides original insights into optimizing analysis workflows, with implications for cost-effective, timely assessments in geoscience and environmental applications.

This study aimed to evaluate the feasibility of using fewer XR-μCT projections to estimate density and porosity in carbonate rocks, aiming to reduce computational time without significantly compromising accuracy. The main objective is to compare XR-μCT and γ-CT techniques in terms of their performance and agreement with reference values. Secondary goals include examining the potential environmental and economic benefits of simplified XR-μCT protocols, such as reduced data volume, faster processing, and suitability for routine applications in reservoir characterization.

Material and Methods

Phantoms for the validation tests

To evaluate the accuracy of the γ-CT and XR-μCT techniques, homogeneous cylindrical phantoms were fabricated from materials of known composition, including aluminum, graphite, acrylic, and water-filled tubes. These materials were chosen because they have known properties similar to those of the samples studied. They serve as references based on their mass attenuation coefficient values, available in the NIST (National Institute of Standards and Technology) XCOM database (Berger et al., 2010). Table 1 shows the chemical compositions, elemental densities, and mass attenuation coefficients at the gamma-ray energy for a ^{241}Am source (59.5 keV) for the materials used as references in this study.

Table 1. Physical and Radiometric Properties of the Phantoms. Font: Carvalho et al. (2024).

Material	Composition	Density ρ (g cm^{-3})	Mass attenuation coefficients μ/ρ (cm^2 g^{-1})
Aluminum	Al – 100%	2.6989	0.2810
Graphite	C – 100%	1.7000	0.1758
Acrylic ($C_5O_2H_8$)	C – 59.98% O – 31.96% H – 8.05%	1.1900	0.1930
Water	H – 66.73%	0.9970	0.2050

(H_2O)	O – 33.37%		

Geological samples of carbonated rocks

The study focused on three carbonate rock samples (Figure 1, Table 2) from the reef limestone outcrop in the Conde municipality, Paraíba, south of the capital, João Pessoa (Nova, 2020). The reef limestone outcrops are situated along the coastal strip and extend approximately 10 km between the beaches of Jacumã and Tambaba (07°21'51" S, 34°47'52" W). The rock samples used were characterized in previous studies using X-ray Fluorescence (XRF) and X-ray Diffraction (XRD) techniques. The samples were determined to contain calcite and dolomite mineral composition (Nova, 2020).


(a) (b) (c)

Figure 1. Carbonate rock samples (a) VN02, (b) VN01, and (c) VN04. Font: Carvalho et al. (2024).

Table 2. Samples of carbonate rocks. Font: Carvalho et al. (2024).

Sample	ρ (g/cm³)	Reference
I (VN02)	2.31	(Nova, 2020)
II (VN01)	2.38	
III (VN04)	2.62	

Gamma-ray computed tomography

Studies using the γ-CT technique on phantoms and geological samples were conducted with a single-beam gamma-ray computed tomography scanner installed at the Department of Nuclear Energy (DEN) of the Federal University of Pernambuco (UFPE). The system comprises a ^{241}Am gamma transmission source with an activity of 7.4×10^9 Becquerel, a half-life of 432.2 years, and a photon energy peak of approximately 59.5 keV. Detection is performed by a NaI(Tl) solid scintillator coupled to a multi-channel analyzer (MCA) model Osprey manufactured by Canberra Inc. Both the source and the detector are equipped with lead collimators, each with a diameter of 5.5 mm and a shielding length of 73 mm. The maximum distance between the source and the detector is 344 mm, as shown in Figure 2.

Figure 2. First-generation gamma-ray computed tomography scanner (TGC - 1st Gen) of the DEN at the UFPE. Font: Carvalho et al. (2024).

The sample to be analyzed for gamma tomography is first prepared by removing any excess material on its surface. Next, the samples are placed on a support tray in the central position, perfectly aligned, between the source and detector systems. After this step, the initial alignment position of the sample is controlled via computer, ensuring that the gamma-ray beam does not interact with the sample but passes close to it. This is done visually using reference markings on the source-base-detector system. Subsequently, the tomography computer is configured to move the sample support base unidirectionally (step size 0.1 mm) perpendicular to the source-detector alignment. This movement is necessary to scan the sample from one end to another. As a result, the gamma tomography records the detected beam intensity at each position, which is saved in a text file.

Microtomography of X-rays

The XR-μCT technique was applied to both phantoms and geological samples using the Nikon Metrology XT H 225 ST industrial scanner. This equipment operates with a maximum power output of 225 W, supporting a voltage of up to 225 kV and a current of up to 1000 μA. The scanner is equipped with a tungsten anode and a 500 μm-thick beryllium window. As shown in Figure 3, the XR-μCT system is composed of four primary components: (1) the X-ray source, (2) the detector, (3) the sample holder, and (4) a computer for data acquisition, image reconstruction, and analysis. The X-ray computed tomography scanner is housed at the X-ray Computed Tomography Laboratory (LTC-RX). This facility is part of the Nuclear Engineering Department (DEN) at the Federal University of Pernambuco (UFPE).

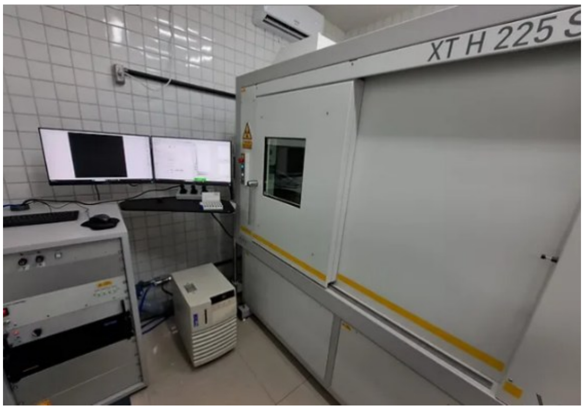

Figure 3. Computed Tomography X-ray Scanner of the DEN at the UFPE. Font: Carvalho et al. (2024).

All samples underwent physical preparation before scanning. The lateral surfaces were manually polished to remove surface irregularities that could interfere with beam attenuation. In addition, the samples were dried in an oven at 60 °C for 24 hours, then stored in a desiccator to maintain a stable moisture content during scanning. The geological and phantom samples were positioned within the tomography scanner and irradiated under consistent conditions using predefined parameters to ensure uniform exposure.

Image reconstruction was performed using the CT Pro 3D software, which included Gaussian smoothing filters and ring artifact correction. Segmentation and porosity quantification were performed using VGStudio Max v3.4, with global thresholding based on the contrast in the grayscale histogram between the matrix and pores. Tomographic projections were then acquired to capture the internal structure of each sample. Lines were drawn on these projections to create grayscale intensity profiles for analysis. These profiles provided measurements of the incident intensity (I0) before passing through the sample and the transmitted intensity (I(x)) detected after interacting with the sample of known thickness ($e_a(x)$). This data was used to apply a set of equations, described in the next section, to calculate the attenuation coefficient (μ), density (ρ), and porosity (ϕ) for both sample types. Figure 4 presents a flowchart outlining the experimental procedure conducted in this study.

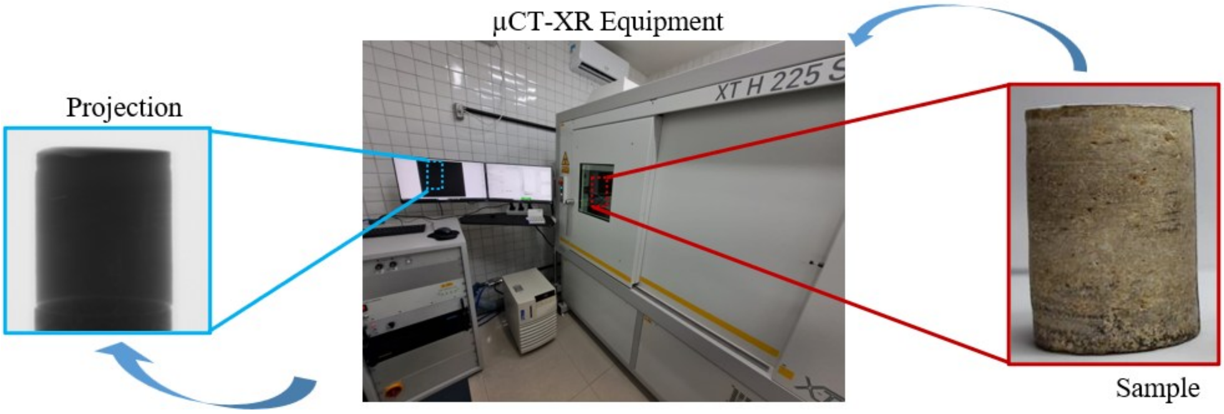

Figure 4. Steps of the experimental procedure for obtaining the variables: μ, ρ, ϕ from one XR-μCT projection. Font: Carvalho et al. (2024).

Mathematical modeling

The mathematical model used to evaluate photon attenuation in matter is based on the Beer-Lambert equation (Equation 1). This equation is widely used in the scientific community to relate incident and transmitted intensities to the attenuation coefficient, thereby describing the interaction of radiation with matter. In the Beer-Lambert equation, “I0” represents the incident radiation intensity, “I” is the transmitted beam intensity, “x” is the path length of the radiation, and “μ” is the linear attenuation coefficient (cm^{-1}). Since this equation is defined for a monochromatic radiation beam, we assume a narrow irradiation geometry, meaning only the transmitted intensity “I” is considered in the transmission measurements (Peak, 2023; Sturrock, 2023).

$$I(x) = I_0 e^{-\mu\, x} \qquad \text{Eq. (1)}$$

The samples undergo gamma ray attenuations, resulting in I(x) and I0, which represent the photon counts transmitted through the sample (or sample container) and the air (or an empty container), respectively. This calculates the relative intensity of gamma transmission across the sample's cross-section (Equation 2).

$$I_\gamma = \frac{I(x)}{I_0} \qquad \text{Eq. (2)}$$

Usually, radiation attenuation in the material is represented independently of the material density by dividing the linear attenuation coefficient “μ” by the density of the material (Equation 3). This coefficient is called the mass linear attenuation coefficient (μ_m).

$$\mu_m = \frac{\mu}{\rho} \qquad \text{Eq. (3)}$$

Equation 4 calculates the material density along the photon path using the mass attenuation coefficient (obtained from the XCOM database) (Dantas et al., 2008; Santos et al., 2011).

$$\rho = -\frac{1}{\mu_m}\ln(I_\gamma)\frac{1}{x} = \frac{1}{\mu_m}\ln\left(\frac{1}{I_\gamma}\right)\frac{1}{x} \qquad \text{Eq. (4)}$$

To determine the μ_m using the XR-μCT projection method, Equation 5 is solved using the X-ray beam intensities at each position of the analyzed projection lines.

$$\mu_m(x) = \frac{1}{e_a(x)\rho}\, ln\left(\frac{I_0}{I(x)}\right), -R_i \le x \le R_i \; \text{Eq. (5)}$$

Finally, for the determination of the porosity using the γ-CT technique, the linear attenuation coefficients of the porous medium (μ) and the material comprising the porous medium (μp) (Equation 6) were employed.

$$\phi = 1 - \frac{\mu}{\mu_p} \qquad \text{Eq. (6)}$$

Two strategies were employed to determine porosity using the XR-μCT technique. The first strategy, which utilized all the obtained projections, employed the Porosity/Inclusion Analysis technique implemented in VGStudio Max version 3.4 image processing and analysis software (Volume Graphics GmbH, 2020) (Figure 5). The second strategy, used for analyses with a single or a set of projections, employed a methodology similar to that used with the gamma transmission technique.

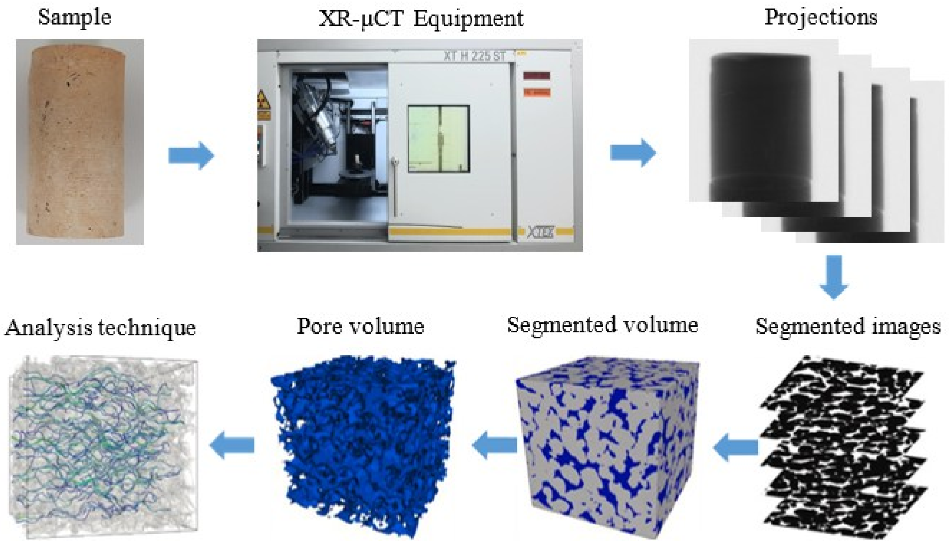

Figure 5. Steps of the experimental procedure and mathematical modeling for obtaining the ϕ from XR-μCT projections utilizing the VGStudio Max image processing and analysis software. Font: Carvalho et al. (2024).

Validation of the γ-CT and XR-μCT techniques

The first step was validating the γ-CT and XR-μCT techniques. Considering this purpose, the radiometric density and mass attenuation coefficient for the four homogeneous material samples were determined. These parameters were then compared with the reference densities of the materials and the values available in the XCOM database. The radiometric density of the samples was determined using Equation 4. In the γ-CT technique, the attenuation coefficient was determined from the gamma-ray tomography intensity values (Figure 6). In contrast, the attenuation coefficient of the XR-μCT technique was calculated from the XR-μCT projection (Figure 7). Table 3 presents the values obtained for the linear attenuation coefficient by the γ-CT and XR-μCT techniques, and Table 4 presents the comparison of the densities obtained by the γ-CT and XR-μCT techniques with the reference densities of the materials.

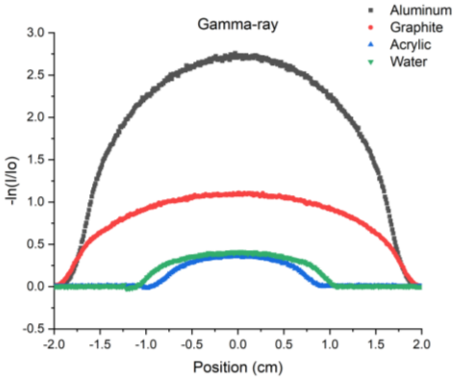

Figure 6. Gamma-ray attenuation obtained by γ-CT for the four homogeneous material samples. Font: Carvalho et al. (2024).

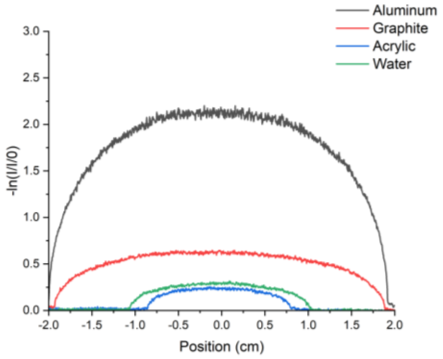

Figure 7. X-ray attenuation obtained by XR-μCT for the four homogeneous material samples. Font: Carvalho et al. (2024).

Table 3. Comparison of the linear attenuation coefficient obtained by the γ-CT and XR-μCT techniques for the four homogeneous material samples. Font: Carvalho et al. (2024).

Sample	**μ (cm^{-1})**	
	μ (γ-CT)	**μ (XR-μCT)**
Aluminum	0.7658	0.5187
Graphite	0.3018	0.2635
Acrylic ($C_5O_2H_8$)	0.2254	0.1954
Water (H_2O)	0.2070	0.1800

As shown in Table 4, validation of the γ-CT and XR-μCT techniques revealed divergent results in density determination using the radiometric methods. The γ-CT technique exhibited good accuracy, with a maximum relative difference of 1.86% for the acrylic sample. In contrast, the XR-μCT technique, which uses only a single projection, yielded results that deviated significantly from the reference values, with a maximum relative difference of -10.65% for the aluminum sample. This discrepancy can be attributed to the complexity of single-projection analysis in XR-μCT. The XR-μCT technique traditionally requires reconstructing multiple projections to generate a three-dimensional image, enabling more precise analysis of the sample's internal structures. Using only a single projection can result in the loss of information about the structure's complexity, limiting the accuracy with which physical properties can be determined.

Table 4. Comparison of densities obtained by the γ-CT and XR-μCT techniques with the reference density for the four homogeneous material samples. RD% represents the relative difference in % between the measured and reference densities. Font: Carvalho et al. (2024).

Sample	**ρ (g cm^{-3})**		
	ρ (Reference)	**ρ (γ-CT) (RD%)**	**ρ (XR-μCT) (RD%)**
Aluminum	2.6989	2.7253 (-0.98%)	2.9863 (-10.65%)
Graphite	1.7000	1.7167 (-0.98%)	1.7267 (-1.57%)
Acrylic ($C_5O_2H_8$)	1.1900	1.1679 (1.86%)	1.1807 (0.79%)
Water (H_2O)	0.9970	1.0725 (-1.28%)	1.0445 (-4.76%)

The next step was to determine the mass attenuation coefficients for the four homogeneous material samples. Table 5 compares the mass linear attenuation coefficients obtained using the γ-CT and XR-μCT techniques with the reference values available in the XCOM database. As expected, given that the mass attenuation coefficient is calculated from linear attenuation coefficient data, the gamma transmission technique yielded satisfactory results. On the other hand, the XR-μCT technique yielded less precise results, with significant deviations from the literature values.

Table 5. Comparison of mass attenuation coefficients obtained by the γ-CT and XR-μCT techniques with the reference mass linear attenuation coefficient for the four homogeneous material samples. RD% represents the relative difference in % between the measured μ/ρ and the μ/ρ of the XCOM database. Font: Carvalho et al. (2024).

Sample	**μ/ρ (cm^2 g^{-1})**			
	μ/ρ (XCOM database) *	**μ/ρ (γ-CT) (RD%)**	**μ/ρ (XCOM database) ****	**μ/ρ (XR-μCT) (RD%)**
Aluminum	0.2810	0.2837 (-0.98%)	0.1737	0.1922 (-10.65%)
Graphite	0.1758	0.1775 (-0.98%)	0.1526	0.1550 (-1.57%)
Acrylic ($C_5O_2H_8$)	0.1930	0.1894 (1.86%)	0.1655	0.1642 (0.79%)
Water (H_2O)	0.2050	0.2076 (-1.28%)	0.1723	0.1805 (-4.76%)

* ^{241}Am - 59.5 keV; ** Effective energy (97.15 keV) obtained from SpekCalc code (Poludniowski et al., 2009).

Results and Discussion

After obtaining unsatisfactory results from homogeneous samples with XR-μCT using only one projection, the question arose whether the poor results were due solely to a single projection or were consistent across multiple projections. Therefore, the first study with carbonate rock samples aimed to evaluate the influence of using just one projection. To do this, the results from a single projection were compared with the averages from two, four, eight, sixteen, and all projections. The model using all projections was assumed to be the most accurate. Table 6 compares the mass attenuation coefficients obtained by the XR-μCT technique with the proposed number of projections and the relative difference with respect to the model with all projections. As shown in Table 6, the results for μ/ρ with only one projection exhibit relative differences compared to the model with all projections that exceed 2%. When using two projections, one sample showed relative differences exceeding 1%. Therefore, four projections were chosen as an acceptable number, yielding results with relative differences of less than 1% compared to those from all projections. This ensures the method's precision regarding the number of projections used; however, it does not guarantee the accuracy of the results. To address this, further comparisons were made with the γ-CT technique and results from the literature.

Table 6. Comparison of mass attenuation coefficients obtained by the XR-μCT technique for the three carbonate rock samples. RD% represents the relative difference in % between the μ/ρ obtained with all the projections and the μ/ρ obtained with a subset of the projections. Font: Carvalho et al. (2024).

Sample	**μ/ρ (cm^2 g^{-1})/ number of projections**					
	All	**16 (RD%)**	**8 (RD%)**	**4 (RD%)**	**2 (RD%)**	**1 (RD%)**
I (VN02)	0.2342	0.2340 (<1)	0.2338 (<1)	0.2326 (<1)	0.2309 (1.44)	0.2291 (2.18)
II (VN01)	0.2298	0.2296 (<1)	0.2294 (<1)	0.2289 (<1)	0.2277 (<1)	0.2255 (1.87)
III (VN04)	0.2255	0.2253 (<1)	0.2250 (<1)	0.2244 (<1)	0.2233 (<1)	0.2197 (2.57%)

The attenuation measurements for the three carbonate rock samples, obtained using both γ-CT and XR-μCT (average of four projections), are illustrated in Figures 8 and 9. The gamma-ray attenuation (Figure 8) and X-ray attenuation (Figure 9) profiles exhibit distinct patterns, reflecting differences in how each technique quantifies the interaction of gamma rays and X-rays with the rock samples. The linear attenuation coefficients, derived from the relative photon-intensity curves for the three samples using both γ-CT and XR-μCT, are presented in Table 7.

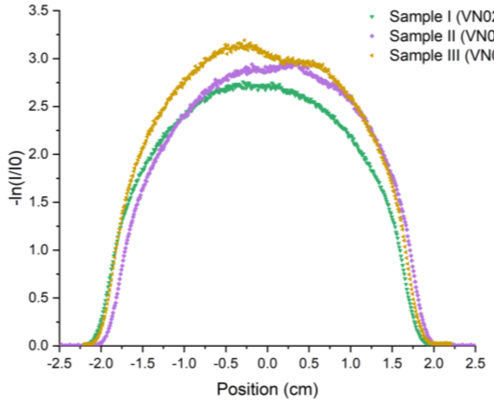

Figure 8. Gamma-ray attenuation obtained by γ-CT for the three carbonate rock samples. Font: Carvalho et al. (2024).

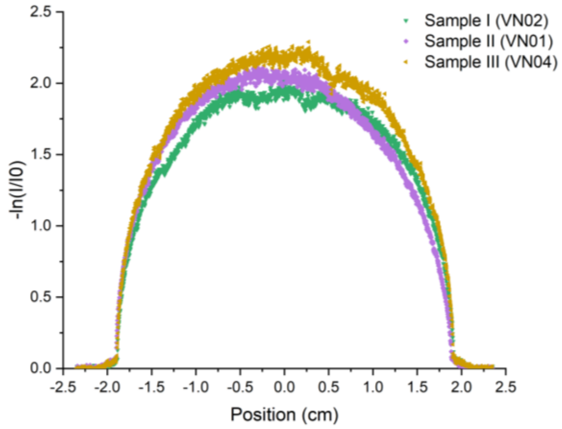

Figure 9. X-ray attenuation obtained by XR-μCT for the three carbonate rock samples. Font: Carvalho et al. (2024).

Table 7. Comparison of linear attenuation coefficients obtained by the γ-CT and XR-μCT techniques for the three carbonate rock samples. Font: Carvalho et al. (2024).

Sample	μ (cm^{-1})	
	μ (γ-CT)	μ (XR-μCT)
I (VN02)	0.7333	0.5288
II (VN01)	0.7525	0.5536
III (VN04)	0.8297	0.5879

The radiometric density and mass attenuation coefficients of the carbonate rock samples were determined from their linear attenuation coefficients. Table 8 presents the density results for the three carbonate rock samples, along with comparisons to the reference densities of the materials. Table 9 presents the mass attenuation coefficients for the three samples, comparing results from γ-CT and XR-μCT with reference values from the XCOM database.

Table 8. Comparison of densities obtained by the γ-CT and XR-μCT techniques with the reference density for the three carbonate rock samples. RD% represents the relative difference in % between the measured and reference densities. Font: Carvalho et al. (2024).

Sample	ρ (g cm^{-3})		
	ρ (Nova, 2020)	ρ (γ-CT) (RD%)	ρ (XR-μCT) (RD%)
I (VN02)	2.31	2.41 (-4.29%)	2.38 (-2.83%)
II (VN01)	2.38	2.48 (-4.21%)	2.49 (-4.73%)
III (VN04)	2.62	2.74 (-4.58%)	2.65 (-1.17%)

Table 9. Comparison of mass attenuation coefficients obtained by the γ-CT and XR-μCT techniques for the three carbonate rock samples. RD% represents the relative difference in % between the measured μ/ρ and the XCOM μ/ρ. Font: Carvalho et al. (2024).

Sample	μ/ρ (cm² g^{-1})			
	μ/ρ (XCOM database) *	μ/ρ (γ-CT) (RD%)	μ/ρ (XCOM database) **	μ/ρ (XR-μCT) (RD%)
I (VN02)	0.3044	0.3174 (-4.29%)	0.2226	0.2289 (-2.83%)
II (VN01)	0.3034	0.3162 (-4.21%)	0.2221	0.2326 (-4.73%)
III (VN04)	0.3028	0.3167 (-4.58%)	0.2218	0.2244 (-1.17%)

* ^{241}Am - 59.5 keV; ** Effective energy (76.94 keV) obtained from SpekCalc code (Poludniowski et al., 2009).

Based on the results presented in Tables 8 and 9, several important conclusions can be drawn regarding the densities and mass attenuation coefficients of the three carbonate rock samples (VN02, VN01, VN04) using the γ-CT and XR-μCT techniques. First, both γ-CT and XR-μCT techniques yielded density values and mass attenuation coefficients close to the reference values, with XR-μCT generally showing smaller relative differences than γ-CT, especially for Sample III. This suggests that XR-μCT may offer slightly better accuracy in density measurements for these carbonate rock samples. Second, unlike homogeneous samples, where XR-μCT results were generally poor, using a few projections (four instead of one) appears to have been effective for rocks. Overall, while both methods are suitable for the radiometric characterization of carbonate rocks, XR-μCT seems to be the more reliable technique (the γ-CT technique always obtained results with differences above 4%), offering more precise measurements that align closely with established reference data.

Table 10 displays the porosity values calculated for the three carbonate rock samples using both the γ-CT and XR-μCT techniques with the two strategies, alongside reference values from earlier studies (Nova, 2020). Table 10 reveals notable differences in the porosity values obtained from the γ-CT technique and the XR-μCT analysis, based on a subset of four projections, compared to the reference values. For Samples I and II (VN02 and VN01), the γ-CT and XR-μCT techniques overestimate porosity between 90% to 160%. For

Sample III (VN04), the results are even worse, significantly overestimating the reference values by more than 300%. This overestimation likely stems from a combination of factors, including the limited spatial resolution of the techniques and the inability of reduced-projection XR-μCT to capture microstructural complexity fully. Additional contributors may include instrumental noise, detector sensitivity, and segmentation artifacts, particularly from automated routines in VGStudio Max, that can blur pore boundaries and inflate pore volume estimates. Mineralogical heterogeneity in carbonate rocks and insufficient detection of fine-scale pore throats can also exacerbate these discrepancies.

Table 10. Comparison of the porosity values obtained by the γ-CT and XR-μCT techniques for the three carbonate rock samples. RD% represents the relative difference in % between the calculated porosities and the reference porosity in Nova (2020). Font: Carvalho et al. (2024).

Sample	**ϕ (%)**			
	Reference ϕ (Nova, 2020)	**ϕ (γ-CT) (RD%)**	**ϕ (XR-μCT) (RD%)**	**ϕ (XR-μCT VGStudio Max) (RD%)**
I (VN02)	16.17	32.96 (-103.80%)	41.08 (-154.06%)	16.34 (-1.05%)
II (VN01)	16.55	32.11 (-94.04%)	39.24 (-137.10%)	16.26 (1.75%)
III (VN04)	6.67	29.13 (-336.67%)	36.95 (-453.99%)	6.64 (0.45%)

From an applied perspective, the implications are significant: porosity values directly influence reservoir modeling, permeability estimates, and resource recovery forecasts. Porosity overestimating by more than 300% could result in substantial errors in volumetric and flow calculations, leading to misguided investment decisions and inefficient exploitation strategies. However, the analysis using VGStudio Max's 3D segmentation approach produced results much closer to reference values, with relative differences under 2%, demonstrating that with adequate resolution and robust segmentation tools, XR-μCT can deliver reliable porosity assessments. Moreover, the use of just four projections, when properly segmented, offers a promising route to reduce computational demands in routine reservoir assessments while balancing efficiency with acceptable accuracy.

Compared to the previous methods, the porosity estimated using the Porosity/Inclusion Analysis technique implemented in VGStudio Max version 3.4 image processing and analysis software was much closer to the reference values, with a maximum relative difference of 1.75%. These findings underscore the importance of considering multiple factors, including sample preparation, imaging parameters, and 3D analysis methods, when evaluating porosity using CT techniques.

Figure 10 presents the segmented 3D images of the carbonate rock samples obtained from XR-μCT, highlighting the internal pore distribution.

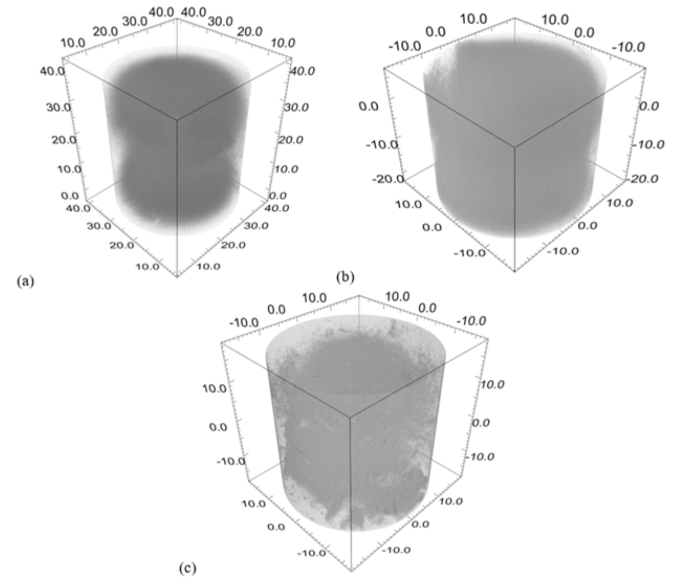

Figure 10. Segmented 3D images with the pore distribution obtained by XR-μCT for the three carbonate rock samples. (a) Sample 1, (b) Sample 2, and (c) Sample 3. Dimensions in millimeters. Font: Carvalho et al. (2024).

It is evident that Samples 1 and 2 exhibit relatively homogeneous porosity patterns, with pores distributed more continuously throughout the matrix. In contrast, Sample 3 shows a markedly heterogeneous pore structure, with clusters of concentrated porosity and regions of low pore connectivity. These spatial patterns are consistent with the quantitative overestimation observed in porosity measurements for Sample 3, suggesting that structural heterogeneity may significantly impact segmentation accuracy and porosity estimation.

Conclusion

This paper demonstrates the applicability of gamma-ray computed tomography (γ-CT) and X-ray microtomography (XR-μCT) for environmental studies, specifically in characterizing the microporosity and density of soils and rocks. The comparative analysis of the γ-CT and XR-μCT techniques demonstrated that both methods can estimate density and porosity in carbonate rock samples, but with notable differences in performance and applicability. The results confirmed that reducing the number of XR-μCT projections can be a viable strategy under specific conditions, particularly when combined with adequate image processing protocols. The study also identified limitations in spatial resolution and segmentation accuracy, underscoring the importance of selecting appropriate techniques and settings for reliable porous media characterization. These findings support the proposed objectives and reinforce the need to adapt tomographic workflows to balance efficiency and reliability.

Acknowledgments

This research was partially supported by the Fundação de Amparo a Ciência e Tecnologia do Estado de Pernambuco (FACEPE), project number BFP-0146-3.09/23, and the Conselho Nacional de Desenvolvimento Científico e Tecnológico (CNPq), project number 465764/2014-2 - Observatório Nacional da Dinâmica da Água e de Carbono no Bioma Caatinga (ONDACBC). The authors also acknowledge CNPq for research support, including the Productivity Fellowship granted to Antonio Celso Dantas Antonino.

References

Abbasi, G. R.; Arif, M.; Isah, A.; Ali, M.; Mahmoud, M.; Hoteit, H.; Keshavarz, A.; Iglauer, S. 2022. Gas hydrate characterization in sediments via x-ray microcomputed tomography. Earth-Science Rev., 234, 104233. https://doi.org/10.1016/j.earscirev.2022.104233

Abdullah, J.; Cassanello, M. C. F.; Dudukovic, M. P.; Dyakowski, T.; Hamada, M. M.; Jin, J. H.; Johansen, G. A.; Kim, J. B.; Legoupil, S. A.; Maad, R.; Mesquita, C.; Nowakowski, J.; Ramirez-Garcia, F. P.; Sankowski, D.; Sipaun, S. M.; Thyn, J. 2008. Industrial Process Gamma Tomography. IAEA-TECDOC-1589. pp. 1-153.

Al-Tersawy, S. H.; El-Sadany, R. A.; Sallam, H. E. M. 2021. Experimental gamma-ray attenuation and theoretical optimization of barite concrete mixtures with nanomaterials against neutrons and gamma rays. Constr. Build. Mater., 289, 123190. https://doi.org/10.1016/j.conbuildmat.2021.123190

Al-Yaseri, A.; Rizwanullah Hussaini, S.; Fatah, A.; Al-Qasim, A. S.; Patil, P. D. 2024. Computerized tomography analysis of potential geochemical reactions of carbonate rocks during underground hydrogen storage. Fuel, 361, 130680. https://doi.org/10.1016/j.fuel.2023.130680

An, R.; Wang, Y.; Zhang, X.; Chen, C.; Liu, X.; Cai, S. 2023. Quantitative characterization of drying-induced cracks and permeability of granite residual soil using micron-sized X-ray computed tomography. Sci. Total Environ., 876, 163213. https://doi.org/10.1016/j.scitotenv.2023.163213

Berger, M. J.; Hubbell, J. H.; Seltzer, S. M.; Chang, J.; Coursey, J. S.; Sukumar, R.; Zucker, D. S.; Olsen, K. 2010. XCOM: Photon Cross Section Database (version 1.5). Available at: http://physics.nist.gov/xcom. Accessed at: 5.23.24).

Bjørnstad, T. 2021. Modern Industry: Gamma Methods for Materials Testing and Inspection. In: Autor. Encyclopedia of Nuclear Energy. Elsevier, pp. 345-371. https://doi.org/10.1016/B978-0-12-819725-7.00142-2

Chirol, C.; Carr, S. J.; Spencer, K. L.; Moeller, I. 2021. Pore, live root and necromass quantification in complex heterogeneous wetland soils using X-ray computed tomography. Geoderma, 387, 114898.

https://doi.org/10.1016/j.geoderma.2020.114898

Cloete, K. J.; Šmit, Ž.; Minnis-Ndimba, R.; Vavpetič, P.; du Plessis, A.; le Roux, S. G.; Pelicon, P. 2019. Physico-elemental analysis of roasted organic coffee beans from Ethiopia, Colombia, Honduras, and Mexico using X-ray micro-computed tomography and external beam particle induced X-ray emission. Food Chemistry: X, 2, 100032. https://doi.org/10.1016/j.fochx.2019.100032

Dantas, C. C.; Melo, S. B.; Oliveira, E. F.; Simões, F. P. M.; Santos, M. G.; Santos, V. A. 2008. Measurement of density distribution of a cracking catalyst in experimental riser with a sampling procedure for gamma ray tomography. Nucl. Instruments Methods Phys. Res. Sect. B Beam Interact. with Mater. Atoms, 266, 841-848. https://doi.org/10.1016/j.nimb.2008.01.029

Fonseca, A. C. G.; Costa, L. F.; Dantas, C. C.; Heck, R. J.; Melo, S. B.; Antonino, A. C. D.; Barbosa, E. S. 2019. Precise determination of soil structure parameters in a X-ray and γ-ray CT combination methodology. Prog. Nucl. Energy, 114, 138-144. https://doi.org/10.1016/j.pnucene.2019.02.007

Freire, L.; Lima, J. S.; Veríssimo, C. U.; Vicente, da S. 2017. Carste em Rochas Não Carbonáticas: contribuição ao estudo geomorfológico em cavernas de arenito da Amazônia Paraense. Rev. Bras. Geogr. Física, 10, 1829-1845.

Galkin, S. V.; Martyushev, D.A.; Osovetsky, B.M.; Kazymov, K.P.; Song, H. 2022. Evaluation of void space of complicated potentially oil-bearing carbonate formation using X-ray tomography and electron microscopy methods. Energy Reports, 8, 6245-6257. https://doi.org/10.1016/j.egyr.2022.04.070

Geiger, J.; Hunyadfalvi, Z.; Bogner, P. 2009. Analysis of small-scale heterogeneity in clastic rocks by using computerized X-ray tomography (CT). Eng. Geol., 103, 112-118. https://doi.org/10.1016/j.enggeo.2008.06.011

Giamas, V.; Koutsovitis, P.; Sideridis, A.; Turberg, P.; Grammatikopoulos, T.A.; Petrounias, P.; Giannakopoulou, P. P.; Koukouzas, N.; Hatzipanagiotou, K. 2022. Effectiveness of X-ray micro-CT applications upon mafic and ultramafic ophiolitic rocks. Micron, 158, 103292. https://doi.org/10.1016/j.micron.2022.103292

Gurin, G.; Ilyin, Y.; Nilov, S.; Ivanov, D.; Kozlov, E.; Titov, K. 2018. Induced polarization of rocks containing pyrite: Interpretation based on X-ray computed tomography. J. Appl. Geophys., 154, 50-63. https://doi.org/10.1016/j.jappgeo.2018.04.019

Jacobs, P.; Cnudde, V. 2009. 'Applications of X-ray computed tomography in engineering geology' or 'looking inside rocks ….'. Eng. Geol., 103, 67-68. https://doi.org/10.1016/j.enggeo.2008.12.001

Khudhur, F. W. K.; MacDonald, J. M.; Daly, L.; Macente, A.; Spruženiece, L.; Griffin, S.; Wilson, C. 2023. Microstructural analysis of slag properties associated with calcite precipitation due to passive CO2 mineralization. Micron, 174, 103532. https://doi.org/10.1016/j.micron.2023.103532

León-Quinto, T.; Madrigal, R.; Cabello, E.; Fimia, A.; Serna, A. 2024. Morphological and biochemical responses of a neotropical pest insect to low temperatures. J. Therm. Biol., 119, 103795. https://doi.org/10.1016/j.jtherbio.2024.103795

Martinez-Garcia, J.; Stelzner, I.; Stelzner, J.; Gwerder, D.; Schuetz, P. 2021. Automated 3D tree-ring detection and measurement from X-ray computed tomography. Dendrochronologia, 69, 125877. https://doi.org/10.1016/j.dendro.2021.125877

Martínez-Martínez, J.; Fusi, N.; Galiana-Merino, J. J.; Benavente, D.; Crosta, G. B. 2016. Ultrasonic and X-ray computed tomography characterization of progressive fracture damage in low-porous carbonate rocks. Eng. Geol., 200, 47-57. https://doi.org/10.1016/j.enggeo.2015.11.009

Martyushev, D. A.; Chalova, P. O.; Davoodi, S.; Ashraf, U. 2023a. Evaluation of facies heterogeneity in reef carbonate reservoirs: A case study from the oil field, Perm Krai, Central-Eastern Russia. Geoenergy Sci. Eng., 227, 211814. https://doi.org/10.1016/j.geoen.2023.211814

Martyushev, D. A.; Davoodi, S.; Kadkhodaie, A.; Riazi, M.; Kazemzadeh, Y.; Ma, T. 2024. Multiscale and diverse spatial heterogeneity analysis of void structures in reef carbonate reservoirs. Geoenergy Sci. Eng., 233, 212569. https://doi.org/10.1016/j.geoen.2023.212569

Martyushev, D. A.; Galkin, S. V.; Shelepov, V. V. 2019. The Influence of the Rock Stress State on Matrix and Fracture Permeability under Conditions of Various Lithofacial Zones of the Tournaisian–Fammenian Oil Fields in the Upper Kama Region. Moscow Univ. Geol. Bull., 74, 573-581. https://doi.org/10.3103/S0145875219060061

Martyushev, D. A.; Ponomareva I. N.; Osovetsky B. M.; Kazymov K. P.; Tomilina E. M.; Lebedeva A. S.; Chukhlov A. S. 2022. Study of the structure and development of oil deposits in carbonate reservoirs using field data and X-ray microtomography. Georesursy, 24, 114-124. https://doi.org/10.18599/grs.2022.3.10

Martyushev, D. A.; Ponomareva, I. N.; Chukhlov, A. S.; Davoodi, S.; Osovetsky, B. M.; Kazymov, K. P.; Yang, Y. 2023b. Study of void space structure and its influence on carbonate reservoir properties: X-ray microtomography, electron microscopy, and well testing. Mar. Pet. Geol., 151, 106192. https://doi.org/10.1016/j.marpetgeo.2023.106192

Melo, A. C.; Bettiol, G.; Barbosa, L.; Augusto, I.; Eyji, E. 2023. Susceptibilidade à erosão, perda de solos e vulnerabilidade natural na bacia do Médio Rio Araguaia - Brasil. Rev. Bras. Geogr. Física, 16, 3103-3124.

Müter, D.; Pedersen, S.; Sørensen, H. O.; Feidenhans'l, R.; Stipp, S. L. S. 2012. Improved segmentation of X-ray tomography data from porous rocks using a dual filtering approach. Comput. Geosci., 49, 131-139. https://doi.org/10.1016/j.cageo.2012.06.024

Nova, A. A. V. 2020. Quantificação da Porosidade em Rochas Calcárias por Meio de Tomografia Computadorizada de Raios X e de Raios Gama. Universidade Federal de Pernambuco. 82p.

Paula, R. T.; Rocha, C. G. 2021. Caracterização Física e Mineralógica de Materiais Intempéricos na Área Urbana de Juiz de Fora – MG, através de Análise Macroscópica, Difratômetro de Raios-X (DRX) e Microscópio Eletrônico de Varredura (MEV). Rev. Bras. Geogr. Física, 14, 1787-1804.

Peak, D. 2023. Fourier transform infrared spectroscopic methods of soil analysis. In: AUTOR. Encyclopedia of Soils in the Environment. Elsevier, pp. 510-518. https://doi.org/10.1016/B978-0-12-822974-3.00230-5

Peters, E. J.; Afzal, N. 1992. Characterization of heterogeneities in permeable media with computed tomography imaging. J. Pet. Sci. Eng., 7, 283-296. https://doi.org/10.1016/0920-4105(92)90024-U

Poludniowski, G.; Landry, G.; DeBlois, F.; Evans, P. M.; Verhaegen, F. 2009. SpekCalc : a program to calculate photon spectra from tungsten anode x-ray tubes. Phys. Med. Biol., 54, N433-N438. https://doi.org/10.1088/0031-9155/54/19/N01

Rahner, M. S.; Halisch, M.; Fernandes, C. P.; Weller, A.; Sampaio, S. S. V. 2018. Fractal dimensions of pore spaces in unconventional reservoir rocks using X-ray nano- and micro-computed tomography. J. Nat. Gas Sci. Eng., 55, 298-311. https://doi.org/10.1016/j.jngse.2018.05.011

Saadat, K.; Rahimpour-Bonab, H. 2023. Lithology determination and petrophysical rock typing of sedimentary rocks using X-ray tomography. Geoenergy Sci. Eng., 231, 212397. https://doi.org/10.1016/j.geoen.2023.212397

Santos, V. A.; Dantas, C. C.; Luna-Finkler, C. L.; Souza, J. E. G. 2011. Principal component analysis in an experimental cold flow model of a fluid catalytic cracking unit by gammametry. Prog. Nucl. Energy, 53, 1114-1118. https://doi.org/10.1016/j.pnucene.2011.06.008

Sturrock, C. J. 2023. Non-invasive imaging of soil processes. In: Goss, M. J.; Oliver, M. (Eds.) Encyclopedia of Soils in the Environment. Elsevier, pp. 459-468. https://doi.org/10.1016/B978-0-12-822974-3.00151-8

Tötzke, C.; Kozhuharova, B.; Kardjilov, N.; Lenoir, N.; Manke, I.; Oswald, S. E. 2024. Non-invasive 3D analysis of microplastic particles in sandy soil - Exploring feasible options and capabilities. Sci. Total Environ., 907, 167927. https://doi.org/10.1016/j.scitotenv.2023.167927

Van Geet, M.; Swennen, R.; Wevers, M. 2000. Quantitative analysis of reservoir rocks by microfocus X-ray computerised tomography. Sediment. Geol. 132, 25-36. https://doi.org/10.1016/S0037-0738(99)00127-X

Volume Graphics GmbH, 2020. VGSTUDIO MAX 3.4 Reference Manual. 34p.